CryoEM Structure of an Influenza Virus Receptor-Binding Site Antibody–Antigen Interface

Yuhang Liu[1,2], Junhua Pan[1], Simon Jenni[3], Donald D. Raymond[1], Tim Caradonna[3], Khoi T. Do[1], Aaron G. Schmidt[1,3], Stephen C. Harrison[1,3,4] and Nikolaus Grigorieff[2,5]

1 - Laboratory of Molecular Medicine, *Boston Children's Hospital, 3 Blackfan Circle, Boston,MA 02115, USA*
2 - Department of Biochemistry, *Brandeis University, 415 South Street, Waltham, MA 02453, USA*
3 - Department of Biological Chemistry and Molecular Pharmacology, *Harvard Medical School, 250 Longwood Avenue, Boston, MA 02115, USA*
4 - Howard Hughes Medical Institute, *Harvard Medical School, Boston, MA 02115, USA*
5 - Howard Hughes Medical Institute, *Janelia Research Campus, Ashburn, VA 20147, USA*

Correspondence to Stephen C. Harrison and Nikolaus Grigorieff:*S. C. Harrison is to be contacted at: Department of Biological Chemistry and Molecular Pharmacology, Harvard Medical School, 250 Longwood Avenue, Boston MA 02115, USA. harrison@crystal.harvard.edu; niko@grigorieff.org*
http://dx.doi.org/10.1016/j.jmb.2017.05.011
Edited by John Johnson

Abstract

Structure-based vaccine design depends on extensive structural analyses of antigen–antibody complexes.Single-particle electron cryomicroscopy (cryoEM) can circumvent some of the problems of x-ray crystallography as a pipeline for obtaining the required structures. We have examined the potential of single-particle cryoEM for determining the structure of influenza-virus hemagglutinin (HA):single-chain variable-domain fragment complexes, by studying a complex we failed to crystallize in pursuing an extended project on the human immune response to influenza vaccines.The result shows that a combination of cryoEM and molecular modeling can yield details of the antigen-antibody interface, although small variation in the twist of the rod-likeHA trimer limited the overall resolution to about 4.5 Å.Comparison of principal 3D classes suggests ways to modify the HA trimer to overcome this limitation. A closely related antibody from the same donor did yield crystals when bound with the same HA, giving us an independent validation of the cryoEM results.The two structures also augment our understanding of receptor-binding site recognition by antibodies that neutralize a wide range of influenza-virus variants.

Introduction

Structure-based vaccine design, made possible by new technologies for generating pathogen-specific human monoclonal antibodies, requires large-scale structural analysis of antigen–antibody complexes [1]. The outlines of the problem have become particularly evident from work on HIV and influenza virus [2]. Single-particle electron cryomicroscopy (cryoEM), which can circumvent some of the problems of x-ray crystallography, has contributed substantially to the study of antibody complexes with the HIV envelope glycoprotein [3,4]. It has helped define epitopes not restricted to the core of the receptor-binding gp120 fragment and establish the relationship of all identifiable epitopes with respect to the trimeric envelope glycoprotein ectodomain.

The trimeric influenza-virus hemagglutinin (HA) ectodomain [5], in association with one antigen-binding fragment (Fab) or single-chain variable-domain fragment (scFv) per subunit, generates a complex with a total mass of 250–300 kDa, well within the range of contemporary, high-resolution cryoEM methods but nonetheless substantially smaller than any comparable HIV gp140:Fab complex. We have examined, in the work described here, the potential of single-particle cryoEM for determining the structure of influenza-virus HA:scFv complexes. In particular, we

describe the structure of a complex we had failed to crystallize, part of a broad study of antibodies from individuals who received the 2007–2008 trivalent inactivated vaccine (TIV) [6]. We compare the result with the crystal structure of the Fab of a closely related antibody from the same donor, bound with the same HA. These antibodies bind HA from nearly all members of a large panel of historical H1 influenza isolates, and a further goal of the studies was to visualize the HA:antibody interface.

The cryoEM structure shows that a combination of cryoEM and molecular modeling can yield details of the antigen:antibody interface.Comparison of principal 3D classes suggests ways to modify the HA trimer to achieve an overall resolution higher than the nominal 4.5 Å of our current reconstruction. The related crystal structure, an independent validation of the cryoEM results, pointed to a local adjustment in the model for the third heavy-chain complementarity region (CDRH3) that improved its agreement with the cryoEM density map.The two structures augment our understanding of receptor-binding site (RBS) recognition by antibodies that neutralize a wide range of influenza-virus variants.

Results

B-cell repertoire of donor TIV24

The HA-directed antibodies we have studied came from a vaccinee who received the 2007–2008 TIV [6]. Paired-chain sequencing of heavy- and light-chain cDNA, from individual B cells obtained 7 days post-vaccination, allowed the expression of recombinant antibodies and, in some cases, the derivation of lineages when more than one sequence derived from the same germline rearrangement was available. Two antibodies, K1912 and K1915, had the same heavy-chain gene rearrangement and very closely related CDRH3s but are paired with a different light chain (Fig.S1). K1912 is one of four antibodies defining a lineage, designated clone 2897 (Fig. S1). Because its light chain is distinct from that of the 2897 clone, K1915 is technically an “orphan” (no other lineage members), but its heavy chain is almost certainly a fifth descendent of the same V(D)J recombination event that led to the clone. The two cDNA sequences are consistent with receptor “revision” after an initial light-chain gene rearrangement [7,8].

Reconstructions from rosettes

We began by considering “rosettes” of intact HA trimers [9] as a way of generating higher image contrast than isolated HAs and aiding particle alignment. HA, solubilized from virions with mild detergent (e.g., β-octyl glucoside) and then dialyzed against detergent-free buffer, associates through its transmembrane segments into small aggregates with the ectodomains projecting radially outwards. We obtained initial, low-resolution results by this approach, but it soon became apparent that new instrumentation and software (in particular, direct detectors, dose fractionation, movie processing, and maximum-likelihood 3D classification) would allow us to reconstruct individual HA ectodomain trimers with bound Fabs. Although we could therefore avoid working with rosettes, the rosette method, modified as described here, helped us obtain an objective starting point for the single-particle analysis of individual Fab:HA complexes. Besides aiding the alignment of small proteins and complexes, this type of approach may also be useful when particles show strongly preferred orientations. By forming rosettes, a broader range of orientations is imposed to allow reconstruction with more isotropic resolution.

Instead of relying on hydrophobic association of transmembrane segments to generate rosettes, we used His-tagged, trimeric HA ectodomain and Ni-NTA-coated gold clusters as nucleation sites. The resulting rosettes are readily recognized in cryoEM images (Fig. 1). The gold clusters allow accurate localization of the rosette centers and help identify side views of individual HA trimers for further processing as single particles. We could usually select two to three single trimers from good clusters (see Materials and Methods). Starting with about 5000 HA trimers thus selected, we used a simple cylinder model as an initial reference (Fig. 1) to perform iterative refinement by projection matching (see Materials and Methods; Fig. S2). Knowledge of the approximate in-plane alignments of the trimers, based on their mean radial direction from the center of the cluster, substantially facilitated projection matching. The prior knowledge of approximate orientation of the 3-fold axis allowed us to exclude particles that deviated significantly from their initial alignments and to calculate a reconstruction at a resolution between 15 and 20 Å (Fig. 1) from a subset of about 3000 trimers. This reconstruction served as an initial model for alignment of HA trimers bound to antibody fragments.

Single-particle reconstruction of HA bound with K1915 antibody fragments

Preliminary studies with the Fab suggested that the constant module, which projected radially, might have enough variability in orientation to compromise refinement of particle parameters. We therefore carried out subsequent studies with the scFv. We collected a large dataset of scFv:HA complexes using a K2 Summit counting detector (Gatan, Inc.) mounted on an FEI Titan Krios electron microscope, operated at 300 kV and 80K (see Materials and Methods). We initially selected about 250,000 particles from 10,280 “movies” and carried out 2D

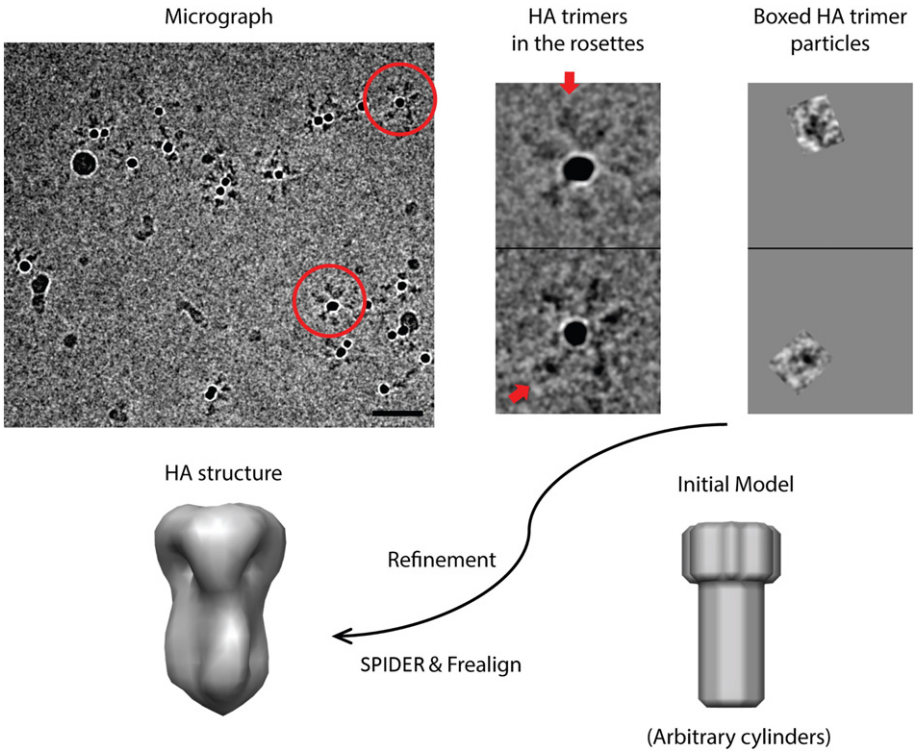

Fig. 1. Use of gold-bead HA rosettes to derive a starting model. Upper row: (left) a field from a cryomicrograph with two rosettes in red circles; scale bar represents 500 Å.(Center) magnified images of those two rosettes, with arrows indicating the HA trimers shown boxed on the right. An arbitrary, cylindrical model (one example shown) led to the low-resolution HA trimer model used for subsequent work.

classification in RELION [10] to detect and remove distorted particles and any that had lost bound scFv (Fig. 2). We aligned the 142,314 particles that passed this filter and calculated a 3D reconstruction with Frealign [11]. Inspection of the resulting map showed that density in the region of the HA stem and head was better defined than the density corresponding to the scFv. We therefore carried out 3D

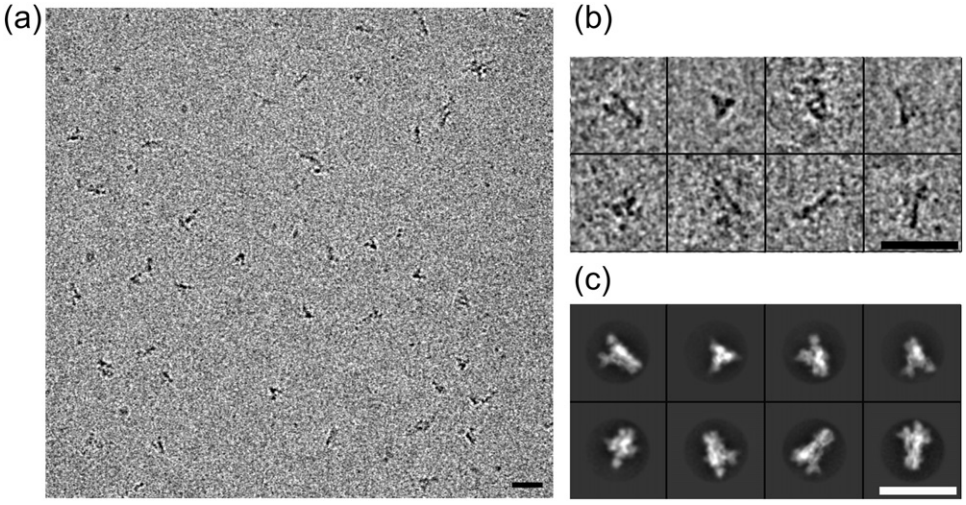

Fig. 2. Examples of results at different data processing stages for the HA:scFv complex. (a) Field from cryomicrograph. (b)Selected particles. (c) 2D class averages showing views both along and normal to the 3-fold axis. The selected particles in (b) belong to the classes in the corresponding positions in (c). Scale bars in (a–c) represent 250 Å.

classification, with four classes, again using Frealign (Fig. 3). Comparing superposed maps from each of the classes revealed that a twist of the complex around its 3-fold axis related one class to another (Figs. 4 and S3). The source of the twisting is not evident, but it could be related to particle distortion during sample freezing or simply to alternative free-energy minima in the trimer, due to the absence of constraints at either end (such as crystallattice contacts or membrane-embedded transmembrane segments). The overall resolution of the reconstructed densities ranged from 4.5 to 6.5 Å (Fig. S4A). Three of the four classes showed high-resolution features with side-chain density in the best-resolved regions (e.g., the central helices of HA). The interface between the scFv and the HA was not as well defined, however, and parts of the scFv distal to the HA interface were even less so, suggesting that four classes may not have captured all conformational states. More classes would have reduced the

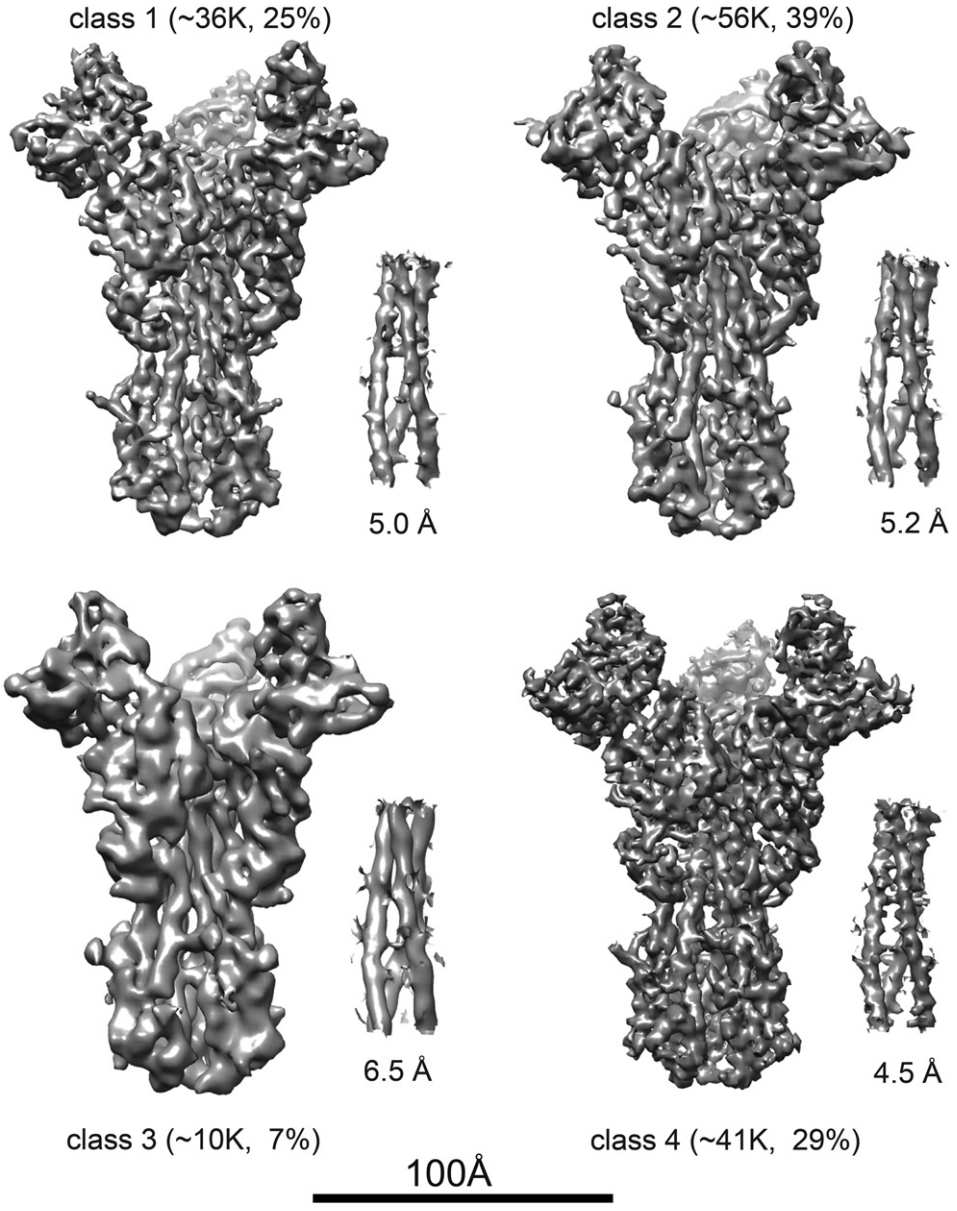

Fig. 3. Surface representations of 3D class averages for the HA:scFv complex. The labels include the number of particles in each class and the corresponding percentage of the total particles included in the computation. Beside each map is a detail from the long central helix of HA_2 to illustrate resolution differences among the classes. The resolutions given are from the half-map FSC for each class (see Fig. S4, which also includes the FSC for each map with its corresponding refined model).

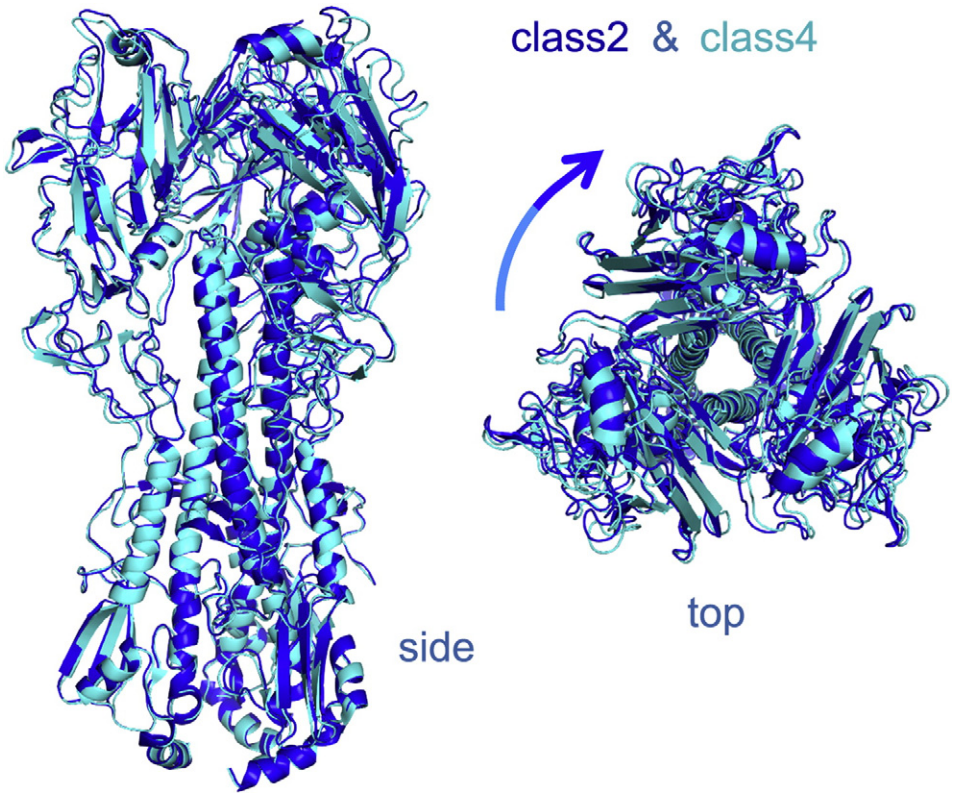

Fig. 4. Superposition of class 2 (blue) and class 4 (cyan) models, illustrating difference in twist around the 3-fold axis. The models were fit to the final reconstructions by real-space refinement, and inspection shows that they accurately represent the key differences between the two maps. The two models are aligned at the base of HA_2, so that a relative circumferential displacement of the upper surface of HA_1 illustrates the overall twist of the molecule. Both views include only the HA part of the model. The top view (right) shows about 10° rotation of one head with respect to the other.

overall definition of the reconstructions owing to the smaller numbers of particles in each class, and we instead attempted to improve the map by local averaging of densities (see next section).

HA:antibody interface of K1915

We averaged density after applying rotational and translational alignments to superpose the densities of the three best classes near the HA:Fv interface, in order to enhance the definition of features in the density map at the antigen–antibody contact. We docked atomic models of HA (from x-ray crystallography) and Fab (from a near homolog) into the density, obtained optimal fits using UCSF Chimera [12], and calculated rigid-body transformations of HA-head:scFv substructures to derive the density-averaging operators. This procedure made the density at the interface somewhat more interpretable (Fig. 5). We assembled a model as described in the next paragraph and adjusted it to fit the map for each of the four classes, using real-space refinement as implemented in Phenix [13] (Table S1).

The model building used the known structure of the H1 A/Solomon Islands/03/2006 HA [14], which we re-refined against reprocessed data (revised PDB deposition 5UGY), and a good homology model for the scFv, from known structures of heavy- and light-chain variable domains with similar sequences (PDB 4K8R). The one segment that required fully de novo modeling was the unusually long CDRH3, which inserts into the HA receptor-binding pocket. Features for several large side chains helped establish an unambiguous sequence register (Fig. 6). The loop folds into the receptor-binding pocket, with some of the features of sialic-acid mimicry we have seen in other RBS-directed antibodies. In particular, the model showed contacts of Val102–Gly103 with Gly135–Ser136 and Trp153 on HA. The valine position and likely non-bonded contacts were like those of the sialic-acid acetamido group, and the glycine carbonyl appeared to occupy the same position as one of the sialic-acid carboxylate oxygens.

Crystal structure of Fab K1912 bound with an HA head domain

We crystallized the Fab of K1912 bound with the Solomon Islands HA head (see Materials and Methods); the crystals yielded a structure of the

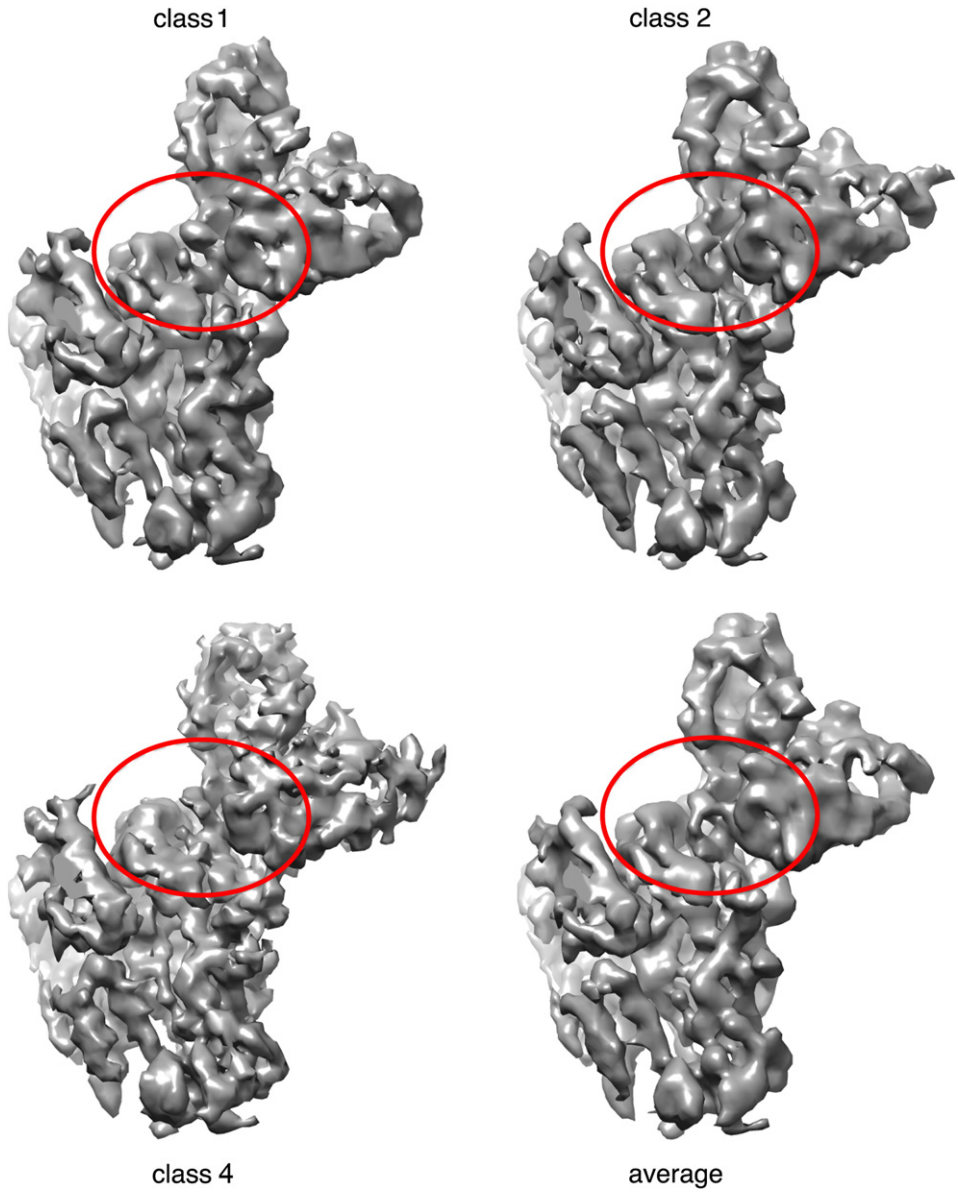

Fig. 5. Density from classes 1,2, and 4 for an HA "head" and bound scFv and average of the three superposed on the region shown in the red ovals. There was a slight enhancement of density at the interface, helpful for building the CDRH3 loop.

complex at 3.4-Å resolution (Fig. 7 and Table S2). Because the CDRH3 sequences of K1915 and K1912 are nearly the same (Fig. S1), we could compare the two structures directly (Fig. S5). Superposition of the electron-microscopy (EM) and x-ray models suggested that a discrepancy in the main-chain fit of the Arg100–Glu101 dipeptide was due to an incorrect modeling of that segment into the EM map. Reconfiguration of that dipeptide, with further small adjustments to reset the fit of CDRH3 to the EM map and subsequent real-space refinement, yielded good agreement with the EM density and an alpha-carbon rmsd of 1.7 Å for 24 residues spanning CDRH3. The largest difference is at the glycine-rich tip of the loop; eliminating just those three residues reduces the rmsd to 1.2 Å. A comparison of structures before and after these adjustments is shown, together with the x-ray structure, in Fig. S5.

RBS recognition

The principal contacts with HA are from the heavy chains of the K1912 and K1915 antibodies, as might be expected from their likely ontogeny (Figs. 7, S1, and S5). In addition to the insertion of CDRH3 into the RBS, there are a set of contacts, both polar and

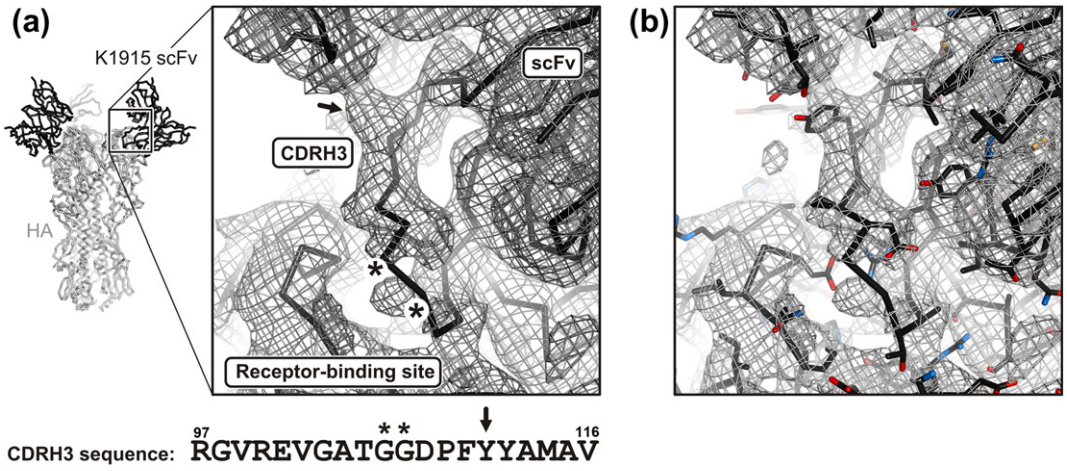

Fig. 6. Conformation of K1915 CDRH3 in the HA receptor-binding site. (a) Backbone trace, with density break at Gly–Gly sequence (asterisks in figure and in sequence below it) and side-chain density for tyrosine (arrow). (b) As in (a), but with side chains.

non-polar, between two residues in CDRH2 and residues 144–145 in HA, and a single van der Waals contact from CDRH1. Light-chain contacts involve just two residues in CDRL1 that are present in the light chains of both antibodies (Tyr32 and Tyr33).

Receptor mimicry by CDRH3 is similar to examples we have described previously [14–16], although the loop itself is substantially longer. Figure 7b illustrates the sialic-acid-like contacts; Fig. S6 shows an explicit comparison of interactions in the K1912 complex with those in a receptor complex. Arg100 (one of the residues adjusted after examining the crystal structure) fixes the conformation of the CDRH3 loop through a network of polar hydrogen bonds with main-chain

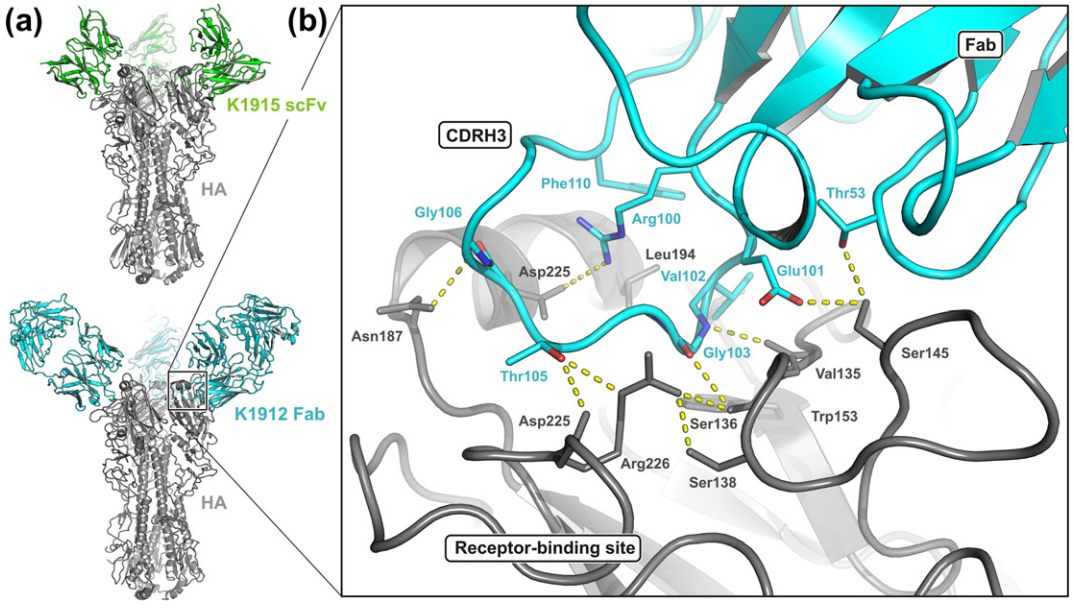

Fig. 7. Receptor-binding site specificity of K1915 and K1912 antibodies. (a) Structures of HA with scFv from antibody K1915 (top), determined by cryoEM, and of K1912 with Fab from antibody K1912 (bottom), determined by x-ray crystallography. HA, gray; K1915 scFv, green; K1912 Fab, blue. See further comparison in Fig. S5. (b) Contacts in the HA sialic-acid binding site. The side chain of Val102 is in the conserved, non-polar pocket bounded by HA residues Trp153, Thr155, and Leu194, into which would insert the methyl group of the receptor acetamido group; a hydrogen bond from the main-chain NH of Gly103 in CDRH3 to the main-chain carbonyl of HA residue 135 resembles a similar bond from the acetamido NH. The carbonyl of Gly103 and the carboxylate of Glu101 have, respectively, polar interactions similar to those of the sialic-acid receptor carboxylate with Ser136 Oγ and Ala137 main-chain NH. Non-polar contacts between the Phe110 side chain and HA Leu194 and between the Gly103 main chain and HA Trp153 resemble contacts from the non-polar surface of the sialic-acid pyranose ring.

carbonyls; thus positioned, the arginine side chain salt-bridges to the carboxylate of Asp190, a conserved residue at the Nterminus of the HA"190s helix".

Residue 226 is Gln in most human H1 isolates, but passage of vaccine strains in chicken eggs can select for a mutation to Arg because of its preference for the avian receptor [16]. In the vaccine-strain Solomon Islands HA we used for crystallization, residue 226 is indeed Arg, which bridges between HA S136 and T105 at the flexible tip of the antibody CDRH3; Gln could do the same (Figs. 7b and S6). Affinities of K1912 for a set of H1 HAs (Fig. S1b) show that binding is essentially indifferent to the substitution. Moreover, both K1912 and K1915 have similar polar contacts with HA residues 226–227, despite their local backbone conformational differences.

Discussion

Receptor mimicry

The long CDRH3 loops of antibodies that recognize the RBS of influenza HA all exhibit some degree of sialic-acid mimicry. The essential HA-receptor contacts are with the sialic-acid carboxylate and acetamido groups and secondarily with the glycerol moiety [5,17]. In the various structures of RBS-directed antibodies bound with HA, groups near the apex of CDRH3 recapitulate most or all of these contacts. The same is true for K1912 and K1915, but with some variations not previously seen. The hydrogen bond between the main-chain amide of Gly103 and the main-chain carbonyl of HA residue 135 and the non-polar contacts of Val 102 with Trp153, Thr 155, and Leu 194 are like the replicas of sialic-acid acetamido group contacts seen in other antibody complexes. Instead of a single acidic residue, however, the side chain of Glu 101 and the main-chain carbonyl of Gly103 share the interactions made in the receptor complex by the sialic-acid carboxylate. The contacts of the antibody with non-conserved residues around the rim of the RBS ignore almost completely the 190s helix, the site of much variation among HAs of influenza isolates [18], except for the salt bridge between Arg 100 and Asp 190; the latter residue is conserved in nearly all H1 influenza HAs in the sequence database. Many of the mutations that lead to escape from neutralization by other RBS-directed antibodies would probably have little effect on K1912 or K1915.

A cryoEM "pipeline" for high-resolution epitope mapping?

Our results illustrate the problems that require solutions before we can depend on cryoEM instead of x-ray crystallography for structures of HA:Fab complexes.The principal limitations appear to be: (1) variation of twist around the long axis of the HA trimer, (2) incomplete scFv occupancy, and (3) preferential particle orientation.

HA twist may be a continuous rather than a discrete variable; a substantially greater number of particles would permit a great number of classes, subdividing the limited range of twists finely enough to achieve higher resolution. The increased speed of image analysis software since completing the work reported here and improved automatic particle-picking routines (e.g., Ref. [19]) will facilitate an efficient pipeline. More particles and hence more classes might also allow the relaxation of 3-fold symmetry at an intermediate stage to eliminate or subclassify particles with less than three bound antibody fragments.

Preferential orientation is a general problem, for which our rosette method is one of many ad hoc solutions.Because the preference is rarely absolute, the problem resembles that of anisotropy in x-ray crystallography, once a reasonable molecular model has been built or fit.Constrained refinement of a model to fit a map of anisotropic resolution can yield a robust result, because stereochemical constraints correlate all three spatial directions.

Materials and Methods

Preparation of influenza HA, K1915 antibody scFv, and K1912 Fab

Recombinant HA (rHA) H1 Solomon Islands/03/2006 (GenBank ABU50586.1) was expressed in *Trichoplusia ni* (Hi-5 cells) using recombinant baculovirus and purified as previously described [14]. The supernatant was harvested and clarified by centrifugation 72 h post-infection. The rHA was purified by immobilized metal affinity chromatography using TALON resin (Clontech). For crystallography, the C-terminal foldon and 6xHis tag were removed using thrombin-conjugated agarose resin (Sigma Aldrich) followed by separation on a Superdex 200 column (GE Healthcare). The resulting rHA was HA_0, with the fusion peptide uncleaved. For cryoEM, when rosettes were not used (see below), the purified rHA was treated for several days at 4 °C with trypsin, resulting in the removal of both the foldon and the 6xHis tag and cleavage between HA_1 and HA_2.

The K1915 scFv and Fab were codon-optimized for mammalian cell expression as previously described [15]. The V_L (residues 1–109) and V_H (residues 1–129) domains were joined using a $(GGGS)_3$ linker and included a non-cleavable, C-terminal 6xHis tag. For expression, 293T cells were transiently transfected using Lipofectamine 2000 (Thermofisher Scientific). Supernatants were harvested 5 days post-transfection, clarified, and isolated on TALON resin (Clontech)

followed by purification over a Superdex 200 column (GE Healthcare). For the Fab, the V_L and V_H were fused to the human C_L (kappa) and C_H domains, respectively, with a non-cleavableC-terminal 6xHis tag on the C_H domain. Equimolar amounts of the heavy- and light-chain plasmids were transiently transfected into 293T cells and purified as described for the scFv.

Preparation of HA rosettes

His-taggedHA solution at a concentration of 0.1 mg/ml was mixed with 10 nM solution of 5 nm Ni-NTA functionalized Nanogold (Nanoprobes). The HA:Nanogold ratio was experimentally optimized to produce rosettes that had about five HA trimers bound per Nanogold particle.

Electron microscopy

Rosette samples were prepared for cryoEM by applying 3 μL of rosette solution to glow-dischargedR 1.2/1.3 holey carbon 200-mesh copper grids (Quantifoil Micro Tools) and plunge-frozen with a Vitrobot Mark I (FEI).We recorded 412 images, with a 1-s exposure of 20 electrons/Å^2, on a US4000 CCD camera (Gatan, Inc.) and an F30 electron microscope (FEI) operated at 300 kV and a nominal magnification of 50,000×, resulting in a calibrated pixel size of 2.2 Å at the specimen level.

HA:scFv cryo samples were prepared in the same way as the rosette samples, after the addition of β-octylglucoside to a final concentration of 0.07% (wt/vol). The detergent prevented a strongly preferred orientation; without it, particles presented views almost exclusively along the symmetry axis. We recorded 10,281 movies on a K2 Summit detector (Gatan, Inc.) and a Titan Krios (FEI) operated at 300 kV and a nominal magnification of 18,000× and controlled by SerialEM[†]; the calibrated physical pixel size was 1.64 Å. We recorded 38 frames/movie in super-resolution mode using an exposure rate of 8electrons/physical pixel/s and a total exposure of 40electrons/Å^2.

Image processing

We selected 9544 HA rosettes manually using e2boxer.py [20], taking special care to center each rosette on the gold clusters. We then picked 5201 suitable HA trimers, again carefully centering on each trimer to obtain rough in-plane orientation angles by connecting the selected locations with the rosette centers. Further processing steps were carried out with the Spider processing software [21]. We boxed and masked each trimer with a rectangular mask aligned with the trimer axis (Fig. 1). We used a cylinder as an initial reference to adjust the alignment of each particle by projection matching and calculated a reconstruction (Fig. S2), iterating seven times. In each iteration, shifts were limited to about 10 Å relative to the original picked positions. Trimers that changed their in-plane rotations by more than 18° or that had a correlation coefficient with their reference projection of less than 0.3 were rejected, leaving 3302 particles in the final reconstruction (Fig. 1) with an estimated resolution of 15 to 20 Å, based on visual inspection of recognizable features.

Frame alignment of movies of the HA:Fv complex was performed with Unblur [22]; frames were summed without exposure filtering. We selected 252,130 particles semi-automatically using e2boxer.py [20]. Particles were boxed and downsampled to 3.28 Å/pixel to accelerate processing. A subset of particles was rejected based on 2D classification using RELION [10], leaving 229,237 particles for 3D analysis. Particles were aligned against the HA trimer reconstruction obtained from the rosettes using projection matching implemented in IMAGIC [23] with a step size of 7.5° and assuming C3 symmetry. Particle alignments were further refined using 10 cycles of Mode 1 in Frealign [11], followed by a few cycles of Mode 2 to align any remaining, incorrectly aligned particles. Frealign 3D classification (two classes) yielded a final dataset of 142,314 particles. Particles in the rejected class appeared to suffer from missing antibody fragments, distortions, and other imperfections. At this point, processing switched to 1.64 Å/pixel downsampled data, and particles were refined further in 60 cycles of Frealign Mode 1, then split into four classes, and refined in another 60 cycles of Mode 1. The resolution limit during processing in Frealign never exceeded 10 Å, and the estimated resolutions of the final four classes were between 4.8 Å and 6.0 Å (Fourier shell correlation, FSC = 0.143 criterion; Fig. S4A). The final maps were scaled in resolution zones against a density map derived from the atomic model of a previously determined structure of HA bound to a different antibody fragment [14]. The scaled maps were then filtered using a figure-of-merit filter [24] based on the estimated FSC curve output by Frealign, adjusted for the volume occupied by the particle (Part_FSC). Finally, the maps were sharpened by a *B*-factor of – 100 A^2.

Model building and refinement for K1915 scFv:HA(A/Solomon Islands/03/2006) complex

We placed the Solomon Islands HA trimer structure (PDB 5UGY) into the EM maps with the programO [25]. For the structure of the K1915 scFv, we used Modeller [26], starting with a structural template from PDB4K8R (chain D residues 1–130 and chain C residues 2–109, corresponding to heavy- and light-chain sequence, respectively). We identified 4K8R as a good template structure for Modeller by

aligning the K1915 sequence to the sequences of all non-redundant structures of the PDB. The heavy and light chains of Fab1 in 4K8R (chains D and C) have 78 and 71% identity with aligned sequences of the corresponding chains in K1915. Using Modeller's automodel class, we generated 10 K1915 models. Superposition of the 10 models showed that they were essentially identical except at the N terminus, the scFv linker, and the CDRH3 loop. Since the conformation of these residues could not be modeled accurately, we removed them before placing the model with the highest molpdf score into the EM map. We then manually built the CDRH3 loop in O, guided by the class 4 EM density, and added N-linked glycans with phenix.carbo_load where supported by density.

We refined coordinates and *B*-factors with phenix.real_space_refine (version 1.11.1–2575, protocol: rigid_body, minimization_global, adp) [13]. In addition to standard geometry and *B*-factor restraints, we applied Ramachandran, rotamer, and secondary structure restraints throughout the refinement. We also used non-crystallographic symmetry torsion angle restraints, thereby essentially imposing 3-fold symmetry on the model, corresponding to the symmetry imposed on the EM reconstruction. The FSCs between the final maps of the four classes and the refined models are shown in Fig. S4B. The estimated resolutions from these analyses (5.1–7.1 Å; FSC = 0.5 criterion) are consistent with the values reported above obtained from the half-map analyses (Fig. S4A). We analyzed the final model with MolProbity [27]; statistics are in Table S1.

Crystallography of K1912 Fab:HA(A/Solomon Islands/03/2006) complex

For crystallization of the K1912 Fab:HA complex, we incubated Fab K1912 with H1 Solomon Islands HA ectodomain at a 1.3:1 M ratio. Complexes were separated from excess K1912 by gel filtration and concentrated to ~22 mg/mL.Hanging-drop vapor diffusion from a 1:1 mixture of the concentrate with reservoir solution containing 10% (wt/vol) polyethylene glycol 8000 and 100 mM Hepes gave crystals of the complex in 3 days at 18 °C. The crystals were cryo-protected by soaking for 5 s in reservoir solution augmented with 15% (vol/vol) 2-methyl-2,4-pentanediol, harvested into loops, and flash-cooled by plunging into liquid N2.

Diffraction data were collected at 100 K on NE-CAT beamline 24-ID-C at the Advanced Photon Source, Argonne National Laboratory (Argonne, IL). Diffraction images were indexed, integrated, and scaled with XDS [28]. Models of Solomon Islands HA (PDB 5UGY) and Fab (PDB 4K8R) were used as probes for molecular replacement with PHASER [29]. Density modification was performed with DM [30], and model rebuilding was completed manually with COOT [31]. Refinement used BUSTER (Global Phasing Ltd). Statistics are in Table S2. Figures were generated with PyMOL (Schrödinger LLC).

Accession numbers

The K1915 scFv:HA electron density maps and the corresponding models of the four classes are deposited in the Electron Microscopy Data Bank (EMDB accession numbers EMD-8561, EMD-8562, EMD-8563, EMD-8564) and Protein Data Bank (PDB accession numbers 5UJZ, 5UK05UK1, 5UK2). The K1912 Fab:HA crystal structure is deposited in the PDB (accession number 5UG0).

Supplementary data to this article can be found online at http://dx.doi.org/10.1016/j.jmb.2017.05.011.

Acknowledgments

We thank Chen Xu (Brandeis University EM Facility), Zongli Li (Harvard Medical School EM Facility), Zhiheng Yu, and Jason de la Cruz (HHMI Janelia Research Campus cryoEM Facility) for technical support, and the NE-CAT beamline staff for help with x-ray data collection.NE-CAT is funded by NIH grant P41 GM-103403 and the Pilatus 6 M detector on 24-ID-C by NIH-ORIPHEI grant S10-RR-029205. APS is operated for the DOE Office of Science by Argonne National Laboratory under contract DE-AC02-06CH11357. The work at Boston Children's Hospital and Harvard Medical School was supported by NIH grants P01 AI-089618 and P01 GM-62580.S.C.H. and N.G. are Investigators in the Howard Hughes Medical Institute.

Received 12 March 2017;
Received in revised form 1 May 2017;
Accepted 9 May 2017
Available online 12 May 2017

Keywords:
electron cryomicroscopy (cryoEM);
x-ray crystallography;
influenza virus hemagglutinin;
antibody binding

Present address: Y. Liu, Pfizer Research and Development, Groton, CT 06340, USA.

†http://bio3d.colorado.edu/SerialEM

Abbreviations used:
cryoEM, electron cryomicroscopy; Env, envelope glycoprotein; HA, hemagglutinin; Fab, antigen-binding fragment; scFv, single-chain variable-domain fragment; TIV, trivalent inactivated vaccine; CDRH3, third heavy-

chain complementarity region; RBS, receptor-binding site; rHA, recombinant HA; EM, electron microscopy; FSC, Fourier shell correlation.

References

[1] R. Rappuoli, M.J. Bottomley, U. D'Oro, O. Finco, E. De Gregorio, Reverse vaccinology 2.0: human immunology instructs vaccine antigen design, J. Exp. Med. 213 (2016) 469–481.

[2] B.F. Haynes, G. Kelsoe, S.C. Harrison, T.B. Kepler, B-cell-lineage immunogen design in vaccine development with HIV-1 as a case study, Nat. Biotechnol. 30 (2012) 423–433.

[3] D. Lyumkis, J.P. Julien, N. de Val, A. Cupo, C.S. Potter, P.J. Klasse, et al., Cryo-EM structure of a fully glycosylated soluble cleaved HIV-1 envelope trimer, Science 342 (2013) 1484–1490.

[4] J.P. Julien, J.H. Lee, G. Ozorowski, Y. Hua, A. Torrents de la Pena, S.W. de Taeye, et al., Design and structure of two HIV-1 clade C SOSIP.664 trimers that increase the arsenal of native-like Env immunogens, Proc. Natl. Acad. Sci. U. S. A. 112 (2015) 11,947–11,952.

[5] J.J. Skehel, D.C. Wiley, Receptor binding and membrane fusion in virus entry: the influenza hemagglutinin, Annu. Rev. Biochem. 69 (2000) 531–569.

[6] M.A. Moody, R. Zhang, E.B. Walter, C.W. Woods, G.S. Ginsburg, M.T. McClain, et al., H3N2 influenza infection elicits more cross-reactive and less clonally expanded anti-hemagglutinin antibodies than influenza vaccination, PLoS One 6 (2011) e25797.

[7] G. Kelsoe, V(D)J hypermutation and receptor revision: coloring outside the lines, Curr. Opin. Immunol. 11 (1999) 70–75.

[8] V. Kouskoff, D. Nemazee, Role of receptor editing and revision in shaping the B and T lymphocyte repertoire, Life Sci. 69 (2001) 1105–1113.

[9] C. Bottcher, K. Ludwig, A. Herrmann, M. van Heel, H. Stark, Structure of influenza haemagglutinin at neutral and at fusogenic pH by electron cryo-microscopy, FEBS Lett. 463 (1999) 255–259.

[10] S.H. Scheres, RELION: implementation of a Bayesian approach to cryo-EM structure determination, J. Struct. Biol. 180 (2012) 519–530.

[11] D. Lyumkis, A.F. Brilot, D.L. Theobald, N. Grigorieff, Likelihood-based classification of cryo-EM images using FREALIGN, J. Struct. Biol. 183 (2013) 377–388.

[12] E.F. Pettersen, T.D. Goddard, C.C. Huang, G.S. Couch, D.M. Greenblatt, E.C. Meng, et al., UCSF chimera—a visualization system for exploratory research and analysis, J. Comput. Chem. 25 (2004) 1605–1612.

[13] P.D. Adams, P.V. Afonine, G. Bunkoczi, V.B. Chen, I.W. Davis, N. Echols, et al., PHENIX: a comprehensive Python-based system for macromolecular structure solution, Acta Crystallogr. D Biol. Crystallogr. 66 (2010) 213–221.

[14] J.R. Whittle, R. Zhang, S. Khurana, L.R. King, J. Manischewitz, H. Golding, et al., Broadly neutralizing human antibody that recognizes the receptor-binding pocket of influenza virus hemagglutinin, Proc. Natl. Acad. Sci. U. S. A. 108 (2011) 14,216–14,221.

[15] A.G. Schmidt, M.D. Therkelsen, S. Stewart, T.B. Kepler, H.X. Liao, M.A. Moody, et al., Viral receptor-binding site antibodies with diverse germline origins, Cell 161 (2015) 1026–1034.

[16] D.D. Raymond, S.M. Stewart, J. Lee, J. Ferdman, G. Bajic, K.T. Do, et al., Influenza immunization elicits antibodies specific for an egg-adapted vaccine strain, Nat. Med. 22 (2016) 1465–1469.

[17] W. Weis, J.H. Brown, S. Cusack, J.C. Paulson, J.J. Skehel, D.C. Wiley, Structure of the influenza virus haemagglutinin complexed with its receptor, sialic acid, Nature 333 (1988) 426–431.

[18] B.F. Koel, D.F. Burke, T.M. Bestebroer, S. van der Vliet, G.C. Zondag, G. Vervaet, et al., Substitutions near the receptor binding site determine major antigenic change during influenza virus evolution, Science 342 (2013) 976–979.

[19] S.H. Scheres, Semi-automated selection of cryo-EM particles in RELION-1.3, J. Struct. Biol. 189 (2015) 114–122.

[20] G. Tang, L. Peng, P.R. Baldwin, D.S. Mann, W. Jiang, I. Rees, et al., EMAN2: an extensible image processing suite for electron microscopy, J. Struct. Biol. 157 (2007) 38–46.

[21] T.R. Shaikh, H. Gao, W.T. Baxter, F.J. Asturias, N. Boisset, A. Leith, et al., SPIDER image processing for single-particle reconstruction of biological macromolecules from electron micrographs, Nat. Protoc. 3 (2008) 1941–1974.

[22] T. Grant, N. Grigorieff, Measuring the optimal exposure for single particle cryo-EM using a 2.6 A reconstruction of rotavirus VP6, Elife 4 (2015) e06980.

[23] M. van Heel, G. Harauz, E.V. Orlova, R. Schmidt, M. Schatz, A new generation of the IMAGIC image processing system, J. Struct. Biol. 116 (1996) 17–24.

[24] C.V. Sindelar, N. Grigorieff, Optimal noise reduction in 3D reconstructions of single particles using a volume-normalized filter, J. Struct. Biol. 180 (2012) 26–38.

[25] T.A. Jones, J.Y. Zou, S.W. Cowan, M. Kjeldgaard, Improved methods for building protein models in electron density maps and the location of errors in these models, Acta Crystallogr. A 47 (1991) 110–119.

[26] B. Webb, A. Sali, Comparative protein structure modeling using MODELLER, Curr. Protoc. Protein Sci. 86 (2016) 2.9.1–2.9.3.7.

[27] V.B. Chen, W.B. Arendall 3rd, J.J. Headd, D.A. Keedy, R.M. Immormino, G.J. Kapral, et al., MolProbity: all-atom structure validation for macromolecular crystallography, Acta Crystallogr. D Biol. Crystallogr. 66 (2010) 12–21.

[28] W. Kabsch, Xds, Acta Crystallogr. D Biol. Crystallogr. 66 (2010) 125–132.

[29] A.J. McCoy, R.W. Grosse-Kunstleve, P.D. Adams, M.D. Winn, L.C. Storoni, R.J. Read, Phaser crystallographic software, J. Appl. Crystallogr. 40 (2007) 658–674.

[30] M.D. Winn, C.C. Ballard, K.D. Cowtan, E.J. Dodson, P. Emsley, P.R. Evans, et al., Overview of the CCP4 suite and current developments, Acta Crystallogr. D Biol. Crystallogr. 67 (2011) 235–242.

[31] P. Emsley, B. Lohkamp, W.G. Scott, K. Cowtan, Features and development of Coot, Acta Crystallogr. D Biol. Crystallogr. 66 (2010) 486–501.

[32] T.B. Kepler, S. Munshaw, K. Wiehe, R. Zhang, J.S. Yu, C.W. Woods, et al., Reconstructing a B-cell clonal lineage. II. Mutation, selection, and affinity maturation, Front. Immunol. 5 (2014) 170.

[33] T.B. Kepler, Reconstructing a B-cell clonal lineage. I. Statistical inference of unobserved ancestors, F1000Res. 2 (2013) 103.

[34] A.G. Schmidt, K.T. Do, K.R. McCarthy, T.B. Kepler, H.X. Liao, M.A. Moody, et al., Immunogenic stimulus for germline precursors of antibodies that engage the influenza hemagglutinin receptor-binding site, Cell Rep. 13 (2015) 2842–2850.